Dynamic Modelling of Dual Three-Phase IPMSM Drives with different Neutral Configurations

Hisham M. Eldeeb, Ayman S. Abdel-Khalik, *Senior Member, IEEE*, Christoph M. Hackl, *Senior Member, IEEE*

***Abstract*—Without prior knowledge of the geometric and design data of the employed asymmetrical dual three-phase interior permanent magnet synchronous machine (ADT-IPMSM), this paper proposes effective fundamental and enhanced harmonic models along with parameter identification for the different subspaces and with different neutral point configurations. The cross-coupling between the coordinates of the different subspaces is also taken into account. The proposed method is based on simple experimental tests which can be applied to any ADT-IPMSMs. The performed computer simulations coincide to a high extent with experimental validations on a 2.5 kW ADT-IPMSM prototype.**

***Index Terms*—Dual three phase, double neutral, IPMSM, modelling, single neutral.**

NOMENCLATURE

Notation

$\mathbb{R}$	Set of real numbers.
$\mathbb{N}$	Set of natural numbers.
n	Number of rows, where $n \in \mathbb{N}$.
m	Number of columns, where $m \in \mathbb{N}$.
ζ	Real scalar, where $\zeta \in \mathbb{R}$.
$\boldsymbol{\zeta}$	Real vector (bold), where $\boldsymbol{\zeta} \in \mathbb{R}^n$.
$\|\|\boldsymbol{\zeta}\|\|$	Euclidean norm of $\boldsymbol{\zeta}$.
$\boldsymbol{Z}$	Real $n \times m$ matrix (capital bold), where $\boldsymbol{Z} \in \mathbb{R}^{n\times m}$.

Subscripts and superscripts

$\square^\top$	Transpose operator applied to either a vector or a matrix.
$\square_{\mathrm{s}}$	Subscript 's' denotes referencing to the stator.
$\square_{\mathrm{s}}^{\lambda}$	Superscript 'λ' is an arbitrary variable representing a subspace (i.e. $\lambda \in \{dq,\, xy,\, 0,\, d_0q_0\}$).
$\square_{\mathrm{s}}^{\Lambda}$	Superscript 'Λ' is an arbitrary variable representing one of the coordinates of λ.

General

$\boldsymbol{I}_n$	Identity matrix, where $\boldsymbol{I}_n \in \mathbb{R}^{n\times n}$.
$\boldsymbol{O}_n$	Zero square matrix, where $\boldsymbol{O}_n \in \mathbb{R}^{n\times n}$.
$\det(\boldsymbol{Q})$	Determinant of a square matrix $\boldsymbol{Q} \in \mathbb{R}^{n\times n}$.
$\boldsymbol{T}_{\mathrm{VSD}}$	Vector space decomposition matrix, where $\boldsymbol{T}_{\mathrm{VSD}} \in \mathbb{R}^{6\times 6}$.
$\boldsymbol{T}_p^{'}$	Generalized Park transformation, where $\boldsymbol{T}_p^{'} \in \mathbb{R}^{6\times 6}$.
$\boldsymbol{T}_p$	Park transformation adopted for three-phase quantities, where $\boldsymbol{T}_p \in \mathbb{R}^{2\times 2}$.
$\boldsymbol{J}$	Rotation matrix, where $\boldsymbol{J} := \boldsymbol{T}_p(\pi/2)^{-1}$.
s	Laplace operator.
$G_{\mathrm{PI}}(s)$	Proportional-integral controller transfer function.
V_p	Proportional gain (Ω).
T_i	Integral time constant (sec).
u	Electrical voltage (V).
i	Electrical current (A).
ψ	Flux linkage (Wb).
$\boldsymbol{\zeta}_{\mathrm{s}}^{a_1\to c_2}$	Stator space vector expressed in the ($\mathrm{a_1b_1c_1}$-$\mathrm{a_2b_2c_2}$) frame, where $\boldsymbol{\zeta} \in \{\boldsymbol{u}, \boldsymbol{\psi}, \boldsymbol{i}\}$).
$\boldsymbol{\psi}_{\mathrm{s,PM}}^{\lambda}$	λ subspace flux linkage harmonic component owing to the PM contribution (Wb).
$\boldsymbol{s}_{\mathrm{VSI}}$	Inverter switching vector.
$\boldsymbol{u}_{\mathrm{s}}^{\mathrm{ph}}$	Inverter phase voltages (V).
$\boldsymbol{u}_{\mathrm{PI}}^{\lambda}$	Control action applied by the PI controller (V).
$\boldsymbol{u}_{\mathrm{R}}^{\lambda}$	Control action applied by the PR controller (V).
$\boldsymbol{u}_{\mathrm{s,dist}}^{\lambda}$	Disturbance feed-forward voltage (V).
u_{dc}	DC-link voltage (V).
m_{e}	Electromechanical torque (N·m).
m_{load}	Load torque (N·m).
n_{p}	Pole-pair number.
ω_{e}	Electrical angular speed (rad/s).
ϕ_{e}	Electrical angular position referred to reference flux axis of phase a_1 (rad).
h	Harmonic order, where $h \in \mathbb{N}$.
ψ_{pm}^{h}	Flux linkage amplitude of the PM h^{th} harmonic (Wb).
ϕ_{o}^{h}	Initial phase angle of the PM h^{th} harmonic (rad).
u_{emf}^{h}	Back-*emf* voltage of the PM h^{th} harmonic (V).
t	Time (s).
Θ	Mechanical inertia (kg·m^2).
R_{s}	Stator electrical resistance (Ω).
$\boldsymbol{L}_{\mathrm{s}}^{\lambda}$	Differential inductance matrix (H).
L_m^{λ}	Cross-coupling inductance between the axes of the λ subspace (H).
L_{s}^{Λ}	Inductance of one of the axes of λ (H).
f_{sw}	Sampling rate (kHz).
t_{sw}	Sampling period, where $t_{\mathrm{sw}} = \frac{1}{f_{\mathrm{sw}}}$ (s).

Manuscript received October 25, 2017; revised January 23, 2018; accepted March 26, 2018.

Hisham M. Eldeeb is with Munich School of Engineering, Technical University of Munich (TUM), in the research group: Control of Renewable Energy Systems (CRES) (e-mail: hisham.eldeeb@tum.de).

A. S. Abdel-Khalik is with Electrical Engineering Department, Faculty of Engineering, Alexandria University, Alexandria 21544, Egypt (e-mail: ayman.abdel-khalik@alexu.edu.eg).

Christoph M. Hackl is with the Munich University of Applied Sciences (MUAS) and head of the CRES research group at TUM (e-mail: christoph.hackl@hm.edu).

I. INTRODUCTION

HIGH power industrial electric machines are accomplished either by increasing the voltage and current ratings of the electric drive (i.e. stator windings and inverter),

increasing the number of phases (i.e. more than three), or both combined. Multiphase machines are an attractive solution; owing to their inherent fault-tolerance capability, enhanced efficiency, rating reduction of the employed voltage source inverter (VSI), and lower torque ripples compared to three phase machines [1]–[6]. Dual three phase machines (DTM) are one of the most common choices, since the windings of three phase machines could be replaced easily by six phase windings for the same stator [3]. A spatial phase shift of $\pi/6$ leads to asymmetrical DTMs (ADTMs), which provides an improved fundamental content of the flux linkage and, thus, lower torque ripples. Modelling of such machines depends mainly on the rotor structure and is crucial in order to specify its capabilities and limitations during normal and faulty conditions as well as ensuring robust control [7]. Asymmetrical dual three phase IPMSMs (ADT-IPMSMs) are of interest; due to their high power to weight ratio and fast dynamics when compared with induction machines [6].

In recent literature concerning the control of an ADT-IPMSM with double neutral (i.e 2N) connection, the different harmonic components in the three subspaces are due to inverter non-idealities, approximated sinusoidal flux distributions from both the stator windings and the rotor permanent magnets. Upon decomposing such harmonics to the different subspaces [8], [9], the compensation techniques with multi-resonant controllers or multi-synchronous frames are adopted till reaching satisfactory results in terms of stator current quality and, hence, torque ripples [2], [9]. However, a clear mathematical model to describe and simulate the machine fundamental-harmonic dynamics is still not clearly stated. Such high fidelity models are essential for instance for the application of model-based controllers, such as finite-control-set model predictive control, which is widely accepted in literature. In [10], the proposed decoupled model relied on the knowledge of machine internal dimensions to perform finite-element (FE) simulations to present the laid out model, showing acceptable agreement between the experimental and simulated results. However, the availability of such information (i.e. dimensions and/or FE data) is not the general case. On the other hand, the single neutral (i.e. 1N) connection has an advantage over the 2N connection in terms of enhancing the fault-tolerance capability [5] and improving the torque density if tied to the DC-link through filter circuits [9]. However, a clear established mathematical model for a 1N connection was scarcely investigated. For either star-connection case (i.e. 1N or 2N), the cross-coupling between the subspace flux linkage elements was neglected. Also, a clear evidence to include or discard the cross-coupling between the non-fundamental subspaces has not been confirmed yet.

This paper demonstrates an effective mathematical model capable of capturing both the fundamental and harmonic dynamics of a practical non-linear ADT-IPMSM with the aid of the experimentally identified flux linkage maps. The method relies on simple tests to identify the different fundamental and harmonic parameters for the different subspaces for the isolated and connected neutral points connection (i.e. 1N and 2N connection). A novel method to identify the zero sequence parameters is illustrated. The cross-coupling between the different subspace flux-linkage elements is identified and taken into account. The computed parameters are inserted into a computer simulation on Matlab/Simulink, where the simulated electrical quantities (i.e. stator current, subspace currents) are compared, at the same conditions, to those obtained from an experimental setup containing a 2.5 kW ADT-IPMSM.

TABLE I. Parameters of the ADT-IPMSM drive.

Parameter	Value
Stator resistance	$R_{\rm s} = 1.1\,\Omega$
Pole-pair	$n_{\rm p} = 3$
Rated stator current	$i_{\rm s,rated} = 4.1$ A
Rated torque	$m_{\rm e,rated} = 10.6$ N·m
Inertia	$\Theta = 0.01$ kg·m^2
Rated mechanical speed	2300 RPM
DC-link voltage	$u_{\rm dc} = 580$ V
Sampling and switching frequencies	$f_{\rm sw} = 8$ kHz

II. Asymmetrical dual three phase drive model

A. Dual three phase IPMSM Model

The dynamic modelling and control in three-phase drives is mostly based on decomposing the three-phase quantities (i.e. voltage, current, and flux linkage) by means of the Clarke's transformation into orthogonal stationary subspaces: the $\alpha\beta$ subspace responsible for the electromechanical modelling and the *zero* subspace represented by the *zero* vector, which exists if a path exists for such component [11]. Applying Park's transformation rotates the stator quantities with the same frequency as the rotor, simplifying the electromechanical model as well as the carried-out control strategy [12].

Similarly, a generalized Clarke's transformation for a DTM drive, also known as vector space decomposition (VSD) [5],

$$\boldsymbol{T}_{\rm VSD} = \frac{1}{3}\begin{bmatrix} 1 & -\frac{1}{2} & -\frac{1}{2} & \frac{\sqrt{3}}{2} & -\frac{\sqrt{3}}{2} & 0 \\ 0 & \frac{\sqrt{3}}{2} & -\frac{\sqrt{3}}{2} & \frac{1}{2} & \frac{1}{2} & -1 \\ 1 & -\frac{1}{2} & -\frac{1}{2} & -\frac{\sqrt{3}}{2} & \frac{\sqrt{3}}{2} & 0 \\ 0 & -\frac{\sqrt{3}}{2} & \frac{\sqrt{3}}{2} & \frac{1}{2} & \frac{1}{2} & -1 \\ 1 & 1 & 1 & 0 & 0 & 0 \\ 0 & 0 & 0 & 1 & 1 & 1 \end{bmatrix}, \tag{1}$$

decomposes the asymmetrical six-phases quantities $\boldsymbol{f}_{\rm s}^{a_1\to c_2}$, where $f \in \{u, \psi, i\}$, to three orthogonal planes $\left(f_{\rm s}^{\alpha\beta},\ f_{\rm s}^{XY},\ f_{\rm s}^{0^+0^-}\right) = \boldsymbol{T}_{\rm VSD}\boldsymbol{f}_{\rm s}^{a_1\to c_2}$, namely the equivalent $\alpha\beta$ subspace, 0^+0^- in the "0" subspace representing the *zero* sequence components from both three-phase sets, and the XY subspace, which directly controls the degree of unbalance between the three-phase sets and derating factors during faults [1], [5], [13]. The VSD matrix maps different harmonics to such subspaces, where $\alpha\beta$ plane holds the $12\gamma\pm1$ harmonics, where $\gamma = \{1, 2, 3, ...\}$, XY is concerned with the $6\gamma \pm 1$ harmonics, where $\gamma = \{1, 3, 5, ...\}$, and 0^+0^- is responsible for the triplets harmonics 3γ, where $\gamma = \{1, 3, 5, ...\}$. Using the generalized Park's transformation [8]

$$\boldsymbol{T}_p^{'}(\phi_{\rm e})^{-1} = \begin{bmatrix} \boldsymbol{T}_p(\phi_{\rm e})^{-1} & \boldsymbol{O}_2 & \boldsymbol{O}_2 \\ \boldsymbol{O}_2 & \boldsymbol{T}_p(-\phi_{\rm e})^{-1} & \boldsymbol{O}_2 \\ \boldsymbol{O}_2 & \boldsymbol{O}_2 & \boldsymbol{I}_2 \end{bmatrix}, \tag{2}$$

TABLE II. Table showing the different connections, control structures and gains used to compute the parameters per subspace.

dq and xy subspaces at 2000 RPM and 2N connection			
PI gains*		PR gains*	
P gain (Ω)	I gain ($\frac{\Omega}{\text{sec}}$)	P gain (Ω)	R gain ($\frac{\Omega}{\text{sec}}$)
dq : 5 xy : 2.5	dq : 5555 xy : 2778	dq : 5 xy : 2.5	dq : 1300 xy : 1300
d_0q_0 subspace at 2000 RPM			
PI gains*		PR gains*	
P gain (Ω)	I gain ($\frac{\Omega}{\text{sec}}$)	P gain (Ω)	R gain ($\frac{\Omega}{\text{sec}}$)
d_0q_0 :3	d_0q_0 :3333	d_0q_0 :3	d_0q_0 : 1300

* Tuned using trial and error.

where $\boldsymbol{T}_p(\phi_\text{e})^{-1} = \begin{bmatrix} \cos(\phi_\text{e}) & -\sin(\phi_\text{e}) \\ \sin(\phi_\text{e}) & \cos(\phi_\text{e}) \end{bmatrix}$, the ADTM-IPMSM dynamic model is

$$\left.\begin{aligned} \boldsymbol{u}_\text{s}^{dq} &= R_\text{s}\,\boldsymbol{i}_\text{s}^{dq} + \omega_\text{e}\,\boldsymbol{J}\boldsymbol{\psi}_\text{s}^{dq} + \tfrac{\text{d}}{\text{d}t}\boldsymbol{\psi}_\text{s}^{dq}, \\ \boldsymbol{u}_\text{s}^{xy} &= R_\text{s}\,\boldsymbol{i}_\text{s}^{xy} - \omega_\text{e}\,\boldsymbol{J}\boldsymbol{\psi}_\text{s}^{xy} + \tfrac{\text{d}}{\text{d}t}\boldsymbol{\psi}_\text{s}^{xy}, \\ \boldsymbol{u}_\text{s}^{0} &= R_\text{s}\,\boldsymbol{i}_\text{s}^{0} + \tfrac{\text{d}}{\text{d}t}\boldsymbol{\psi}_\text{s}^{0}, \\ \tfrac{\Theta}{n_\text{p}}\tfrac{\text{d}\omega_\text{e}}{\text{d}t} &= \underbrace{3\,n_\text{p}\boldsymbol{i}_\text{s}^{dq\top}\boldsymbol{J}\,\boldsymbol{\psi}_\text{s}^{dq}}_{:=m_\text{e}} - m_\text{load}, \end{aligned}\right\} \quad (3)$$

where $\boldsymbol{i}_\text{s}^{dq} = \begin{pmatrix} i_\text{s}^d, & i_\text{s}^q \end{pmatrix}^\top$, $\boldsymbol{i}_\text{s}^{xy} = \begin{pmatrix} i_\text{s}^x, & i_\text{s}^y \end{pmatrix}^\top$, and $\boldsymbol{i}_\text{s}^{0} = \begin{pmatrix} i_\text{s}^{0^+}, & i_\text{s}^{0^-} \end{pmatrix}^\top$. $\boldsymbol{\psi}_\text{s}^{dq} = \begin{pmatrix} \psi_\text{s}^d, & \psi_\text{s}^q \end{pmatrix}^\top$, $\boldsymbol{\psi}_\text{s}^{xy} = \begin{pmatrix} \psi_\text{s}^x, & \psi_\text{s}^y \end{pmatrix}^\top$, and $\boldsymbol{\psi}_\text{s}^{0} = \begin{pmatrix} \psi_\text{s}^{0^+}, & \psi_\text{s}^{0^-} \end{pmatrix}^\top$ are the flux linkages in the three decoupled subspaces, which are modelled as shown in the next subsection. In (3), $\boldsymbol{\psi}_\text{s}^{xy} = \boldsymbol{\psi}_{\text{s,f}}^{xy} + \boldsymbol{\psi}_{\text{s,PM}}^{xy}$, represents the total flux linkage in the xy subspace, which is the sum of the fundamental and harmonic flux linkage components, respectively; owing to the non-ideal properties of drive as explained later in Subsect. II-B2. The dq subspace is assumed to posses only the fundamental component; since higher harmonics - namely the 11 and 13 harmonics - are of negligible amplitudes. The ADT-IPMSM parameters are shown in Table I. Since the xy plane rotates in the anti-synchronous frame, a negative sign is placed for the position and speed in (2) and (3), respectively [4]. The model in (3) assumes non-linear flux linkage variations with the corresponding currents. Thus, in this paper, the flux linkages are used as *states* instead of currents. Also, a clear harmonic model, dependent on the permanent magnet (PM) harmonic flux distribution, is proposed and capable of reproducing the results obtained from the practical ADT-IPMSM, as explained in the upcoming subsections.

B. Non-linear Flux Linkage and Harmonic Models

The unique difference between different ADTMs is the way the flux linkage vectors in (3) are modeled. Compared to the laid out models in [9], [10], [14], the current-dependency of inductance matrices as well as harmonic flux linkages per subspace are considered in the proposed model. The objective is to excite the stator windings with the desired subspace currents and identify the corresponding flux linkages, without provoking the remaining subspaces as shown next.

1) dq subspace flux linkages: The torque equation (3) is dependent on the $\boldsymbol{\psi}_\text{s}^{dq}$, which is *ideally* linearly proportional to $\boldsymbol{i}_\text{s}^{dq}$. Practically, this assumption does not hold and a cross-coupling between the $\boldsymbol{\psi}_\text{s}^{dq}$ elements do exist. This is mathematically modelled as $\frac{\text{d}}{\text{d}t}\boldsymbol{\psi}_\text{s}^{dq} = \boldsymbol{L}_\text{s}^{dq}(\boldsymbol{i}_\text{s}^{dq})\,\frac{\text{d}}{\text{d}t}\boldsymbol{i}_\text{s}^{dq}$, where $\boldsymbol{L}_\text{s}^{dq}(\boldsymbol{i}_\text{s}^{dq}) = \begin{bmatrix} \frac{\partial\psi_\text{s}^d}{\partial i_\text{s}^d} & \frac{\partial\psi_\text{s}^d}{\partial i_\text{s}^q} \\ \frac{\partial\psi_\text{s}^q}{\partial i_\text{s}^d} & \frac{\partial\psi_\text{s}^q}{\partial i_\text{s}^q} \end{bmatrix} = \begin{bmatrix} L_\text{s}^d(\boldsymbol{i}_\text{s}^{dq}) & L_m^{dq}(\boldsymbol{i}_\text{s}^{dq}) \\ L_m^{dq}(\boldsymbol{i}_\text{s}^{dq}) & L_\text{s}^q(\boldsymbol{i}_\text{s}^{dq}) \end{bmatrix}$ is the differential inductance matrix (non-linear and current-dependant[1]). This mathematical approach is similar to the that shown in [16], which is also known as the flux linkage maps identification. $\boldsymbol{\psi}_\text{s}^{dq}$ is estimated at a 2N connection (see Figs. 1 and 2), to eliminate the effect of $\boldsymbol{i}_\text{s}^0$, where the current vector $\boldsymbol{i}_\text{s}^{dq}$ is varied to cover the entire operating range of the adopted ADT-IPMSM at a given speed. The reference currents $\boldsymbol{i}_{\text{s,ref}}^{xy}$, shown in Fig 1, are set to $\boldsymbol{i}_{\text{s,ref}}^{xy} = (0,\,0)$. The control action $\boldsymbol{u}_\text{R}^{dq}$ of the proportional-resonant (PR) controller in Fig. 1 ensures equal current amplitudes in both three-phase sets [8]. Accordingly, at *steady-state* using the control structure in

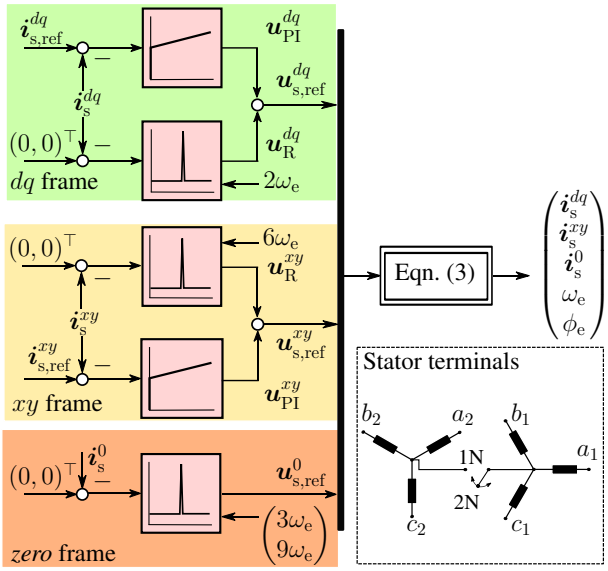

Fig. 1. Proportional-integral and resonant current controllers for the different subspaces with the corresponding resonant frequencies [8], [9].

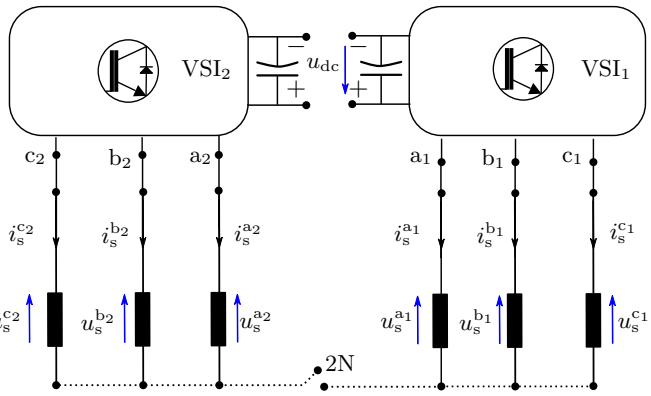

Fig. 2. Hardware configuration for parameters identification of the dq and xy subspaces with isolated neutrals.

[1] Details on nonlinear modelling and the use of differential inductances in electrical drives can be found in [15, Chap. 14].

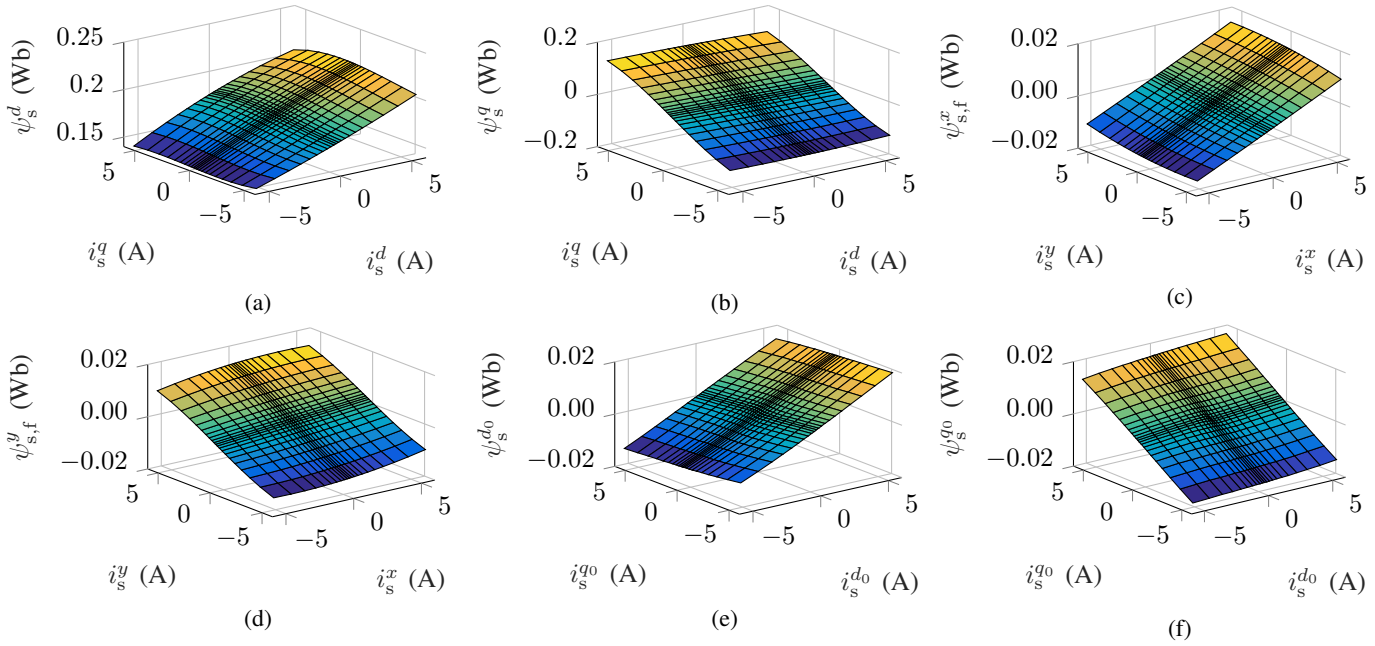

Fig. 3. Measured flux linkage maps of {(a),(b)} $\boldsymbol{\psi}_s^{dq}$ for different $\boldsymbol{i}_s^{dq}$, {(c),(d)} $\boldsymbol{\psi}_s^{xy}$ for different $\boldsymbol{i}_s^{xy}$, and {(e),(f)} $\boldsymbol{\psi}_s^{d_0q_0}$ for different $\boldsymbol{i}_s^0$.

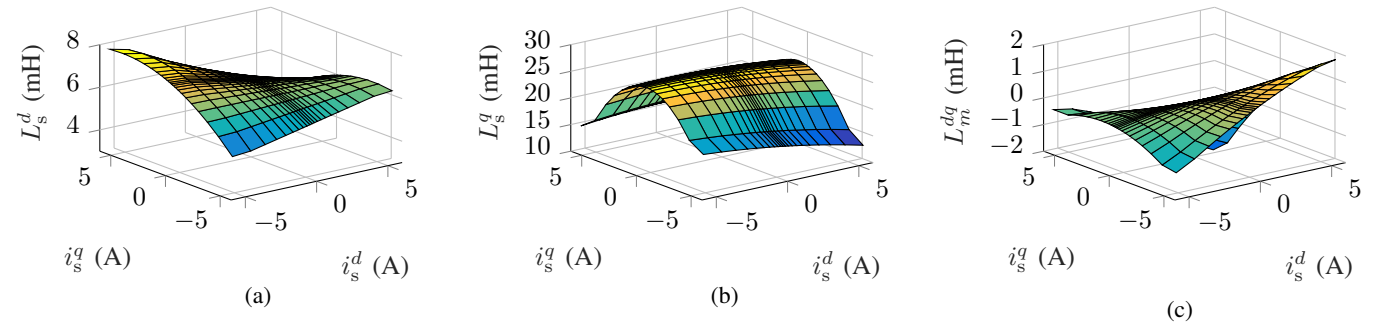

Fig. 4. Measured differential inductances of (a) L_s^d (b) L_s^q (c) L_m^{dq} within the domain $||\boldsymbol{i}_s^{dq}|| \leq i_{s,\text{rated}}$.

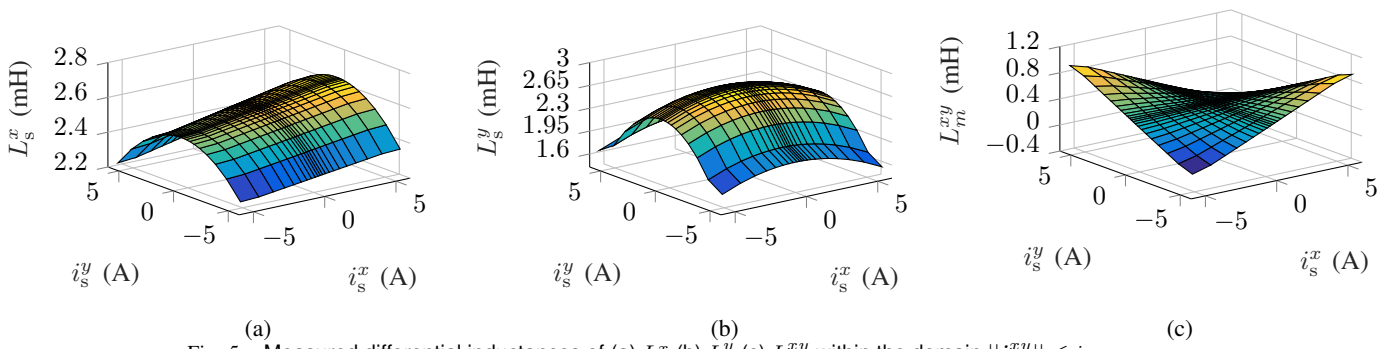

Fig. 5. Measured differential inductances of (a) L_s^x (b) L_s^y (c) L_m^{xy} within the domain $||\boldsymbol{i}_s^{xy}|| \leq i_{s,\text{rated}}$.

Fig. 1, the flux linkage vector is

$$\boldsymbol{\psi}_s^{dq} = \frac{\boldsymbol{J}^{-1}}{\omega_e}(\boldsymbol{u}_{PI}^{dq} - R_s\,\boldsymbol{i}_s^{dq}), \tag{4}$$

where $\boldsymbol{u}_{PI}^{dq}$ is the control action of the proportional-integral (PI) controller (see Fig. 1). Note that the ADT-IPMSM rotates by means of an external prime mover as seen later in Sect. IV. It is clear that the adopted method is valid only at $\omega_e \neq 0$. The acquired flux linkages and the corresponding differential inductances are shown in Figs. 3(a)-(b) and Figs. 4(a)-(c), respectively, through 11 points variations per i_s^d and i_s^q within the domains $-i_{s,\text{rated}} \leq i_s^d \leq i_{s,\text{rated}}$ and $-i_{s,\text{rated}} \leq i_s^q \leq i_{s,\text{rated}}$. Consequently, the flux linkages and inductances are stored as 11×11 look-up tables, which is considered as compromise between accuracy, precision and memory requirements based on the available lab facilities. The PI and PR controllers are initially tuned using trial and error as presented in Table II. Later in Sect. III, the PI controller will employ the computed $\boldsymbol{\psi}_s^{dq}$ and $\boldsymbol{L}_s^{dq}$ in achieving fast dynamic response. For simplified notation, the argument $\boldsymbol{i}_s^{dq}$ is dropped from L_s^d, L_s^q, L_m^{dq}.

2) xy subspace flux linkages: The 5^{th} and 7^{th} harmonics are considered the significant dominant harmonics in such plane, sourced by the rotor harmonics; owing to PM rotor

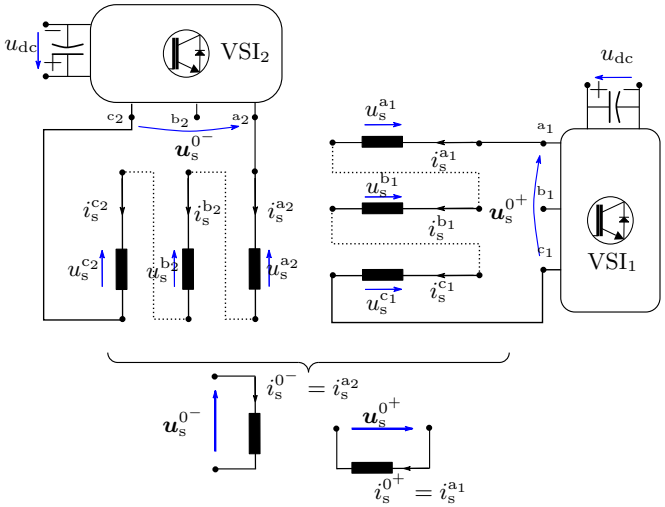

Fig. 6. Hardware configuration for parameters identification of the zero frame flux linkages showing the equivalent two-phase circuit.

flux harmonics. The PM harmonic flux linkage in the xy subspace $\boldsymbol{\psi}^{xy}_{\mathrm{s,PM}}$, which will be presented shortly, is the main enhancement within the xy subspace model. The flux linkage $\boldsymbol{\psi}^{xy}_{\mathrm{s}}$ models the unbalance between the fundamental components of the two-three phase sets [4], [8], which is identified by using the same control structure shown in Figs. 1 and hardware connection in Fig. 2 at a 2N connection. In this case, upon sweeping the current vector $\boldsymbol{i}^{xy}_{\mathrm{s}}$, the flux linkages at *steady-state* and for $\boldsymbol{i}^{dq}_{\mathrm{s,ref}} = (0,\,0)$ can be computed by

$$\boldsymbol{\psi}^{xy}_{\mathrm{s,f}} = -\frac{\boldsymbol{J}^{-1}}{\omega_{\mathrm{e}}}\,(\boldsymbol{u}^{xy}_{\mathrm{PI}} - R_{\mathrm{s}}\,\boldsymbol{i}^{xy}_{\mathrm{s}}), \tag{5}$$

where the harmonic currents produced by $\boldsymbol{\psi}^{xy}_{\mathrm{s,PM}}$ are suppressed by means of PR controllers tuned at $6\omega_{\mathrm{e}}$ [8]. Controller gains are set as presented in Table II. $\boldsymbol{\psi}^{xy}_{\mathrm{s}}$ can be expressed in terms of the fundamental xy differential inductance matrix $\boldsymbol{L}^{xy}_{\mathrm{s}}$, similar to that in Subsect. II-B1. Hence, $\frac{\mathrm{d}}{\mathrm{d}t}\boldsymbol{\psi}^{xy}_{\mathrm{s,f}} = \boldsymbol{L}^{xy}_{\mathrm{s}}(\boldsymbol{i}^{xy}_{\mathrm{s}})\,\frac{\mathrm{d}}{\mathrm{d}t}\boldsymbol{i}^{xy}_{\mathrm{s}}$, where $\boldsymbol{L}^{xy}_{\mathrm{s}}(\boldsymbol{i}^{xy}_{\mathrm{s}}) = \begin{bmatrix} \frac{\partial\psi^{x}_{\mathrm{s,f}}}{\partial i^{x}_{\mathrm{s}}} & \frac{\partial\psi^{x}_{\mathrm{s,f}}}{\partial i^{y}_{\mathrm{s}}} \\ \frac{\partial\psi^{y}_{\mathrm{s,f}}}{\partial i^{x}_{\mathrm{s}}} & \frac{\partial\psi^{y}_{\mathrm{s,f}}}{\partial i^{y}_{\mathrm{s}}} \end{bmatrix} = \begin{bmatrix} L^{x}_{\mathrm{s}} & L^{xy}_{m} \\ L^{xy}_{m} & L^{y}_{\mathrm{s}} \end{bmatrix}$ is the differential inductance matrix in the xy subspace, showing variable L^{x}_{s} and L^{y}_{s} with relative coupling between the xy coordinates represented by L^{xy}_{m} (argument $\boldsymbol{i}^{xy}_{\mathrm{s}}$ is dropped). ψ^{x}_{s} and ψ^{y}_{s} are shown in Figs. 3(c)-(d), while the elements of $\boldsymbol{L}^{xy}_{\mathrm{s}}(\boldsymbol{i}^{xy}_{\mathrm{s}})$ are shown in Figs. 5(a)-(b). The maps are obtained within the domain $-i_{\mathrm{s,rated}} \le i^{x}_{\mathrm{s}} \le i_{\mathrm{s,rated}}$ and $-i_{\mathrm{s,rated}} \le i^{y}_{\mathrm{s}} \le i_{\mathrm{s,rated}}$ with the same number of points as in Subsect. II-B1.

Since the xy subspace encompasses the rotor 5^{th} and 7^{th} harmonics, applying Park's transformation in (2) maps such harmonics to the xy plane rotating at $6\omega_{\mathrm{e}}$. The proposed model for such harmonics is

$$\boldsymbol{\psi}^{xy}_{\mathrm{s,PM}} = \begin{pmatrix} \psi^{7^{\mathrm{th}}}_{\mathrm{pm}}\,\sin(6\omega_{\mathrm{e}}t + \phi^{7^{\mathrm{th}}}_{\mathrm{o}}) - \psi^{5^{\mathrm{th}}}_{\mathrm{pm}}\,\sin(6\omega_{\mathrm{e}}t + \phi^{5^{\mathrm{th}}}_{\mathrm{o}}) \\ \psi^{7^{\mathrm{th}}}_{\mathrm{pm}}\,\cos(6\omega_{\mathrm{e}}t + \phi^{7^{\mathrm{th}}}_{\mathrm{o}}) + \psi^{5^{\mathrm{th}}}_{\mathrm{pm}}\,\cos(6\omega_{\mathrm{e}}t + \phi^{5^{\mathrm{th}}}_{\mathrm{o}}) \end{pmatrix} \tag{6}$$

where the constants $\psi^{5^{\mathrm{th}}}_{\mathrm{pm}}$, $\psi^{7^{\mathrm{th}}}_{\mathrm{pm}}$, $\phi^{5^{\mathrm{th}}}_{\mathrm{o}}$, and $\phi^{7^{\mathrm{th}}}_{\mathrm{o}}$ are identified through the open circuit test as explained in Subsect. II-B4.

3) zero *subspace flux linkages:* The *zero* sequence components flow upon connecting the 1N connection shown in Fig. 1. Since the *zero* sequence components are by nature stationary, the shown control structure in Fig. 1 makes it impossible to sweep $\boldsymbol{i}^{0}_{\mathrm{s}}$ through all the possible values, as in Subsects. II-B1 and II-B2; since the available degrees of freedoms in such 1N connection permits only $i^{0^+}_{\mathrm{s}} = -i^{0^-}_{\mathrm{s}}$. Furthermore, the pulsating behaviour of zero sequence elements obstructs the rotation of the control frame to create the corresponding flux linkage maps. In order to sweep all the possible values for $\boldsymbol{i}^{0}_{\mathrm{s}}$, the proposed circuitry in Fig. 6 allows the flow of only $\boldsymbol{i}^{0}_{\mathrm{s}}$ within the stator terminals, by connecting the phases per three-phase set in series. This is confirmed by equating the currents within the same three-phase set and substituting in (1). A parallel connection of the windings as shown in [7] is not suitable for ADT-IPMSMs; since the back-emf will permit the flow of $\boldsymbol{i}^{dq}_{\mathrm{s}}$ within the windings along with $\boldsymbol{i}^{0}_{\mathrm{s}}$ which is undesirable to obtain $\boldsymbol{\psi}^{0}_{\mathrm{s}}$. In Fig. 6, the machine is transformed to an equivalent balanced two-phase machine (i.e. $i^{0^+}_{\mathrm{s}}$ and $i^{0^-}_{\mathrm{s}}$ are orthogonal) with $3n_{\mathrm{p}}$ equivalent electrical number of pole pairs. $\boldsymbol{i}^{0}_{\mathrm{s}}$ is transformed to their corresponding d_0q_0 components (i.e. $\boldsymbol{i}^{d_0q_0}_{\mathrm{s}}$) by applying $\boldsymbol{T}_p(3\phi_{\mathrm{e}})$. Accordingly, a simplified closed loop controller is proposed to regulate $\boldsymbol{i}^{d_0q_0}_{\mathrm{s}}$, which is shown in Fig. 7, enabling the sweep of $\boldsymbol{i}^{d_0q_0}_{\mathrm{s}}$ and computing the corresponding $\boldsymbol{\psi}^{d_0q_0}_{\mathrm{s}}$ shown in Figs. 3(e)-(f), within the domain $-i_{\mathrm{s,rated}} \le i^{d_0}_{\mathrm{s}} \le i_{\mathrm{s,rated}}$ and $-i_{\mathrm{s,rated}} \le i^{q_0}_{\mathrm{s}} \le i_{\mathrm{s,rated}}$ similar to the cases in Subsects. II-B1 and II-B2. In Fig. 7, a compensation of the 9^{th} and 15^{th} harmonics, rotating at $6\omega_{\mathrm{e}}$ and $12\omega_{\mathrm{e}}$, was implemented to enhance the quality of $\boldsymbol{i}^{d_0q_0}_{\mathrm{s}}$ during the post-processing for computing $\boldsymbol{\psi}^{d_0q_0}_{\mathrm{s}}$. Using that connection along with the corresponding tuning shown in Table II, the voltages can be modulated as

$$\underbrace{\left(u^{\mathrm{a1}}_{\mathrm{s,ref}},\quad u^{\mathrm{c1}}_{\mathrm{s,ref}},\quad u^{\mathrm{a2}}_{\mathrm{s,ref}},\quad u^{\mathrm{c2}}_{\mathrm{s,ref}}\right)^{\top}}_{:=\boldsymbol{u}^{\mathrm{ph}}_{0,\mathrm{ref}}} = \underbrace{\frac{3}{2}\begin{bmatrix} 1 & 0 \\ -1 & 0 \\ 0 & 1 \\ 0 & -1 \end{bmatrix}}_{:=\boldsymbol{T}_{\mathrm{mod}}}\boldsymbol{u}^{0}_{\mathrm{s,ref}}, \tag{7}$$

while $\boldsymbol{\psi}^{d_0q_0}_{\mathrm{s}}$ is computed by

$$\boldsymbol{\psi}^{d_0q_0}_{\mathrm{s}} = \frac{\boldsymbol{J}^{-1}}{3\omega_{\mathrm{e}}}\,(\boldsymbol{u}^{d_0q_0}_{\mathrm{PI}} - R_{\mathrm{s}}\,\boldsymbol{i}^{d_0q_0}_{\mathrm{s}}). \tag{8}$$

The elements of the differential inductance $\boldsymbol{L}^{d_0q_0}_{\mathrm{s}}(\boldsymbol{i}^{d_0q_0}_{\mathrm{s}})$ are plotted in Fig. 8(a)-(c), which show that $L^{d_0}_{\mathrm{s}}$ and $L^{q_0}_{\mathrm{s}}$ variate within $\approx \pm 13\%$ from their origin points and relatively small coupling inductance $L^{d_0q_0}_{m}$ (argument $\boldsymbol{i}^{d_0q_0}_{\mathrm{s}}$ is dropped). Accordingly, coming back to the 1N connection, $\boldsymbol{\psi}^{0}_{\mathrm{s}}$ in the presented pulsating *zero* frame in (3) can be modelled as

$$\boldsymbol{\psi}^{0}_{\mathrm{s}} \;=\; \boldsymbol{L}^{0}_{\mathrm{s}}\,\boldsymbol{i}^{0}_{\mathrm{s}} + \boldsymbol{\psi}^{0}_{\mathrm{s,PM}}, \tag{9}$$

where $\boldsymbol{L}^{0}_{\mathrm{s}}$ is approximated to a constant inductance matrix and defined as $\boldsymbol{L}^{0}_{\mathrm{s}} = \begin{bmatrix} \mathrm{mean}(L^{d_0}_{\mathrm{s}}) & 0 \\ 0 & \mathrm{mean}(L^{q_0}_{\mathrm{s}}) \end{bmatrix}$, while the proposed PM contribution to the zero sequence flux linkage is

$$\boldsymbol{\psi}^{0}_{\mathrm{s,PM}} = \begin{pmatrix} \psi^{3^{\mathrm{rd}}}_{\mathrm{pm}}\,\sin(3\omega_{\mathrm{e}}t + \phi^{3^{\mathrm{rd}}}_{\mathrm{o}}) + \psi^{9^{\mathrm{th}}}_{\mathrm{pm}}\,\sin(9\omega_{\mathrm{e}}t + \phi^{9^{\mathrm{th}}}_{\mathrm{o}}) \\ \psi^{3^{\mathrm{rd}}}_{\mathrm{pm}}\,\cos(3\omega_{\mathrm{e}}t + \phi^{3^{\mathrm{rd}}}_{\mathrm{o}}) + \psi^{9^{\mathrm{th}}}_{\mathrm{pm}}\,\cos(9\omega_{\mathrm{e}}t + \phi^{9^{\mathrm{th}}}_{\mathrm{o}}) \end{pmatrix}. \tag{10}$$

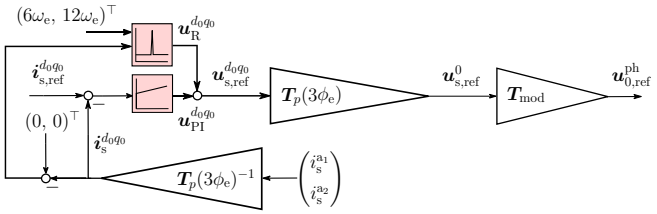

Fig. 7. Controller block diagram for the connection in Fig. 6.

TABLE III. Rotor flux linkage constants at 2000 RPM.

Order	Magnitude (Wb)	Phase (rad)
1	180×10^{-3}	0
3	$\psi_{\rm pm}^{3^{\rm rd}} = 6.6 \times 10^{-3}$	$\phi_{\rm o}^{3^{\rm rd}} = 0.0297$
5	$\psi_{\rm pm}^{5^{\rm th}} = 5 \times 10^{-3}$	$\phi_{\rm o}^{5^{\rm th}} = 3.3755$
7	$\psi_{\rm pm}^{7^{\rm th}} = 4.7 \times 10^{-3}$	$\phi_{\rm o}^{7^{\rm th}} = 0.2077$
9	$\psi_{\rm pm}^{9^{\rm th}} = 4 \times 10^{-3}$	$\phi_{\rm o}^{9^{\rm th}} = 0.4398$

The constants in (10) are identified as explained in Subsect. II-B4. Finally, the equivalent circuits for the proposed models in the xy and zero frames are shown in Fig. 9.

4) Harmonic PM constants identification: To identify the constants in (6) and (10), the ADT-IPMSM was rotated using an external prime mover (see Fig. 11) at a constant speed of 2000 RPM while the ADT-IPMSM was open circuited. Using Fast Fourier transform (FFT), the flux-linkage of the $h^{\rm th}$ harmonic was derived from the back-*emf* as

$$\psi_{\rm pm}^{h} = \text{Amplitude}\big(\frac{u_{emf}^{h}}{h\,\omega_{\rm e}}\big), \tag{11}$$

leading to the results shown in Table III. The initial phase angles $\phi_{\rm o}^{h}$ in Table III were given by the Fourier analyses with respect to the fundamental component. Finally a summary of the required tests to identify the different ADT-IPMSM parameters is demonstrated in the flowchart shown in Fig. 10.

C. Dual three-phase two-level Inverter Model

The number of independent currents to be controlled are *four* for the 2N configuration and *five* for the 1N connection. Assuming balanced phase voltages, the VSI phase voltages $\boldsymbol{u}_{\rm s}^{\rm ph} := \big(u_{\rm s}^{\rm a_1},\ u_{\rm s}^{\rm b_1},\ u_{\rm s}^{\rm c_1},\ u_{\rm s}^{\rm a_2},\ u_{\rm s}^{\rm b_2},\ u_{\rm s}^{\rm c_2}\big)^\top$ can be expressed for 2N as [17]

$$\boldsymbol{u}_{\rm s}^{\rm ph} = \frac{u_{\rm dc}}{3}\begin{bmatrix} 2 & -1 & -1 & 0 & 0 & 0 \\ -1 & 2 & -1 & 0 & 0 & 0 \\ -1 & -1 & 2 & 0 & 0 & 0 \\ 0 & 0 & 0 & 2 & -1 & -1 \\ 0 & 0 & 0 & -1 & 2 & -1 \\ 0 & 0 & 0 & -1 & -1 & 2 \end{bmatrix} \boldsymbol{s}_{\rm VSI}, \tag{12}$$

and for 1N [18]

$$\boldsymbol{u}_{\rm s}^{\rm ph} = \frac{u_{\rm dc}}{6}\begin{bmatrix} 5 & -1 & -1 & -1 & -1 & -1 \\ -1 & 5 & -1 & -1 & -1 & -1 \\ -1 & -1 & 5 & -1 & -1 & -1 \\ -1 & -1 & -1 & 5 & -1 & -1 \\ -1 & -1 & -1 & -1 & 5 & -1 \\ -1 & -1 & -1 & -1 & -1 & 5 \end{bmatrix} \boldsymbol{s}_{\rm VSI}, \tag{13}$$

where $\boldsymbol{s}_{\rm VSI} := \big(s_{\rm VSI}^{\rm a_1},\ s_{\rm VSI}^{\rm b_1},\ s_{\rm VSI}^{\rm c_1},\ s_{\rm VSI}^{\rm a_2},\ s_{\rm VSI}^{\rm b_2},\ s_{\rm VSI}^{\rm c_2}\big)^\top$ is the switching vector such that its elements represent the switching state per phase $s_{\rm VSI}^{\kappa} \in \{0, 1\}$ and $\kappa \in \{\rm a_1,\ b_1, ...,\ c_2,\}$, where the values 0 and 1 indicate that the upper switch is turned OFF or ON, respectively, while the opposite applies to the lower switch. Inverter switching imperfectness as well as other sources of non-idealities such as dead-time have been neglected in the employed simulations, which will be shown later in Sect. IV.

III. ADT-IPMSM Current controller

The control structure for ADT-IPMSMs in Fig. 1 is similar to that in [4], [6], [8] in terms of the invoked assumptions, that the PI controllers in the dq and xy subspaces deal with the fundamental component (see $\boldsymbol{u}_{\rm PI}^{dq}$ and $\boldsymbol{u}_{\rm PI}^{xy}$ in Fig. 1), while the PR controllers deal solely with the harmonic current components. Thus, upon computing the flux linkage maps and the corresponding differential inductances, the PI controllers in Fig. 1 are designed according to the magnitude optimum criterion along with updating the PI controller gain and time constant [16]. Accordingly, by defining the transfer function of a PI controller as

$$G_{\rm PI}(s) = V_p(1 + \frac{1}{T_i\, s}), \tag{14}$$

the proportional and integral time constant of the non-linear PI controllers in the dq and xy frames are tuned as

$$\left.\begin{aligned} \big(V_p^d,\ V_p^q,\ V_p^x,\ V_p^y\big) &= \tfrac{1}{2t_{\rm sw}}\big(\hat{L}_{\rm s}^d,\ \hat{L}_{\rm s}^q,\ \hat{L}_{\rm s}^x,\ \hat{L}_{\rm s}^y\big), \\ \big(T_i^d,\ T_i^q,\ T_i^x,\ T_i^y\big) &= \tfrac{1}{R_{\rm s}}\big(\hat{L}_{\rm s}^d,\ \hat{L}_{\rm s}^q,\ \hat{L}_{\rm s}^x,\ \hat{L}_{\rm s}^y\big), \end{aligned}\right\} \tag{15}$$

where

$$\left.\begin{aligned} \big(\hat{L}_{\rm s}^d,\quad \hat{L}_{\rm s}^q\big) &= \det\big(\boldsymbol{L}_{\rm s}^{dq}(\boldsymbol{i}_{\rm s}^{dq})\big)\Big(\tfrac{1}{L_{\rm s}^q},\quad \tfrac{1}{L_{\rm s}^d}\Big), \\ \big(\hat{L}_{\rm s}^x,\quad \hat{L}_{\rm s}^y\big) &= \det\big(\boldsymbol{L}_{\rm s}^{xy}(\boldsymbol{i}_{\rm s}^{xy})\big)\Big(\tfrac{1}{L_{\rm s}^y},\quad \tfrac{1}{L_{\rm s}^x}\Big). \end{aligned}\right\} \tag{16}$$

In [16], the disturbance feedforward compensation enhances the tracking speed of the PI controllers. The disturbance voltage $\boldsymbol{u}_{\rm s,dist}^{dq}$ encompasses the coupling terms between the dq frame coordinates, assuming the machine parameters are identified, which is the case here upon computing $\boldsymbol{\psi}_{\rm s}^{dq}$ and $\boldsymbol{L}_{\rm s}^{dq}(\boldsymbol{i}_{\rm s}^{dq})$. As proven in [16], $\boldsymbol{u}_{\rm s,dist}^{dq}$ is computed by

$$\boldsymbol{u}_{\rm s,dist}^{dq} = -L_m^{dq}\begin{bmatrix} 0 & \frac{1}{\hat{L}_{\rm s}^q} \\ \frac{1}{\hat{L}_{\rm s}^d} & 0 \end{bmatrix}(\boldsymbol{u}_{\rm s}^{dq} - R_{\rm s}\,\boldsymbol{i}_{\rm s}^{dq} - \omega_{\rm e}\,\boldsymbol{J}\boldsymbol{\psi}_{\rm s}^{dq}) - \omega_{\rm e}\,\boldsymbol{J}\boldsymbol{\psi}_{\rm s}^{dq}. \tag{17}$$

Similarly, the coupling between the xy subspaces can be decoupled using a similar approach as in (17) leading to

$$\boldsymbol{u}_{\rm s,dist}^{xy} = -L_m^{xy}\begin{bmatrix} 0 & \frac{1}{\hat{L}_{\rm s}^y} \\ \frac{1}{\hat{L}_{\rm s}^x} & 0 \end{bmatrix}(\boldsymbol{u}_{\rm s}^{xy} - R_{\rm s}\,\boldsymbol{i}_{\rm s}^{xy} - \omega_{\rm e}\,\boldsymbol{J}\boldsymbol{\psi}_{\rm s}^{xy}) + \omega_{\rm e}\,\boldsymbol{J}\boldsymbol{\psi}_{\rm s}^{xy}. \tag{18}$$

From (15)-(18), the PI controllers with constant tuning in Fig. 1 are replaced with non-linear PI controllers, where both $\boldsymbol{u}_{\rm s,dist}^{dq}$ and $\boldsymbol{u}_{\rm s,dist}^{xy}$ are not shown but inserted within closed loop PI controller blocks.

The presence of undesired harmonics per subspace contributes to significant torque ripples and acoustic noise as well as additional copper losses. This infers the necessity of employing PR controllers to mitigate such effect. To ensure a zero steady-state error per subspace, the resonant (R) part of the digital PR controller must be carefully implemented. Unlike the employed PR controller in [8], this paper discretize the continuous R controller using the impulse invariant method, ensuring a correct lock on the desired resonant frequency [9]. The R controllers time constants in the dq and xy subspaces

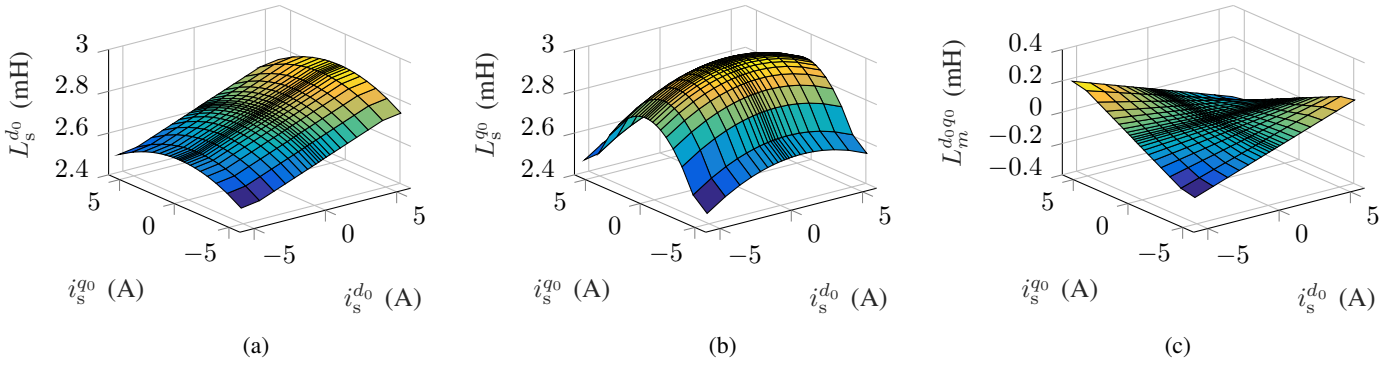

Fig. 8. Measured differential inductances of (a) $L_{\mathrm{s}}^{d_0}$ (b) $L_{\mathrm{s}}^{q_0}$ (c) $L_m^{d_0q_0}$ within the domain $||\boldsymbol{i}_{\mathrm{s}}^{d_0q_0}|| \leq i_{\mathrm{s,rated}}$.

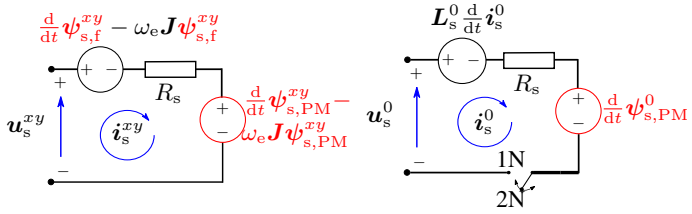

Fig. 9. Equivalent circuits for the fundamental xy and *zero* frames along with highlighting in red the enhanced model elements as explained in Subsects. II-B2 and II-B3.

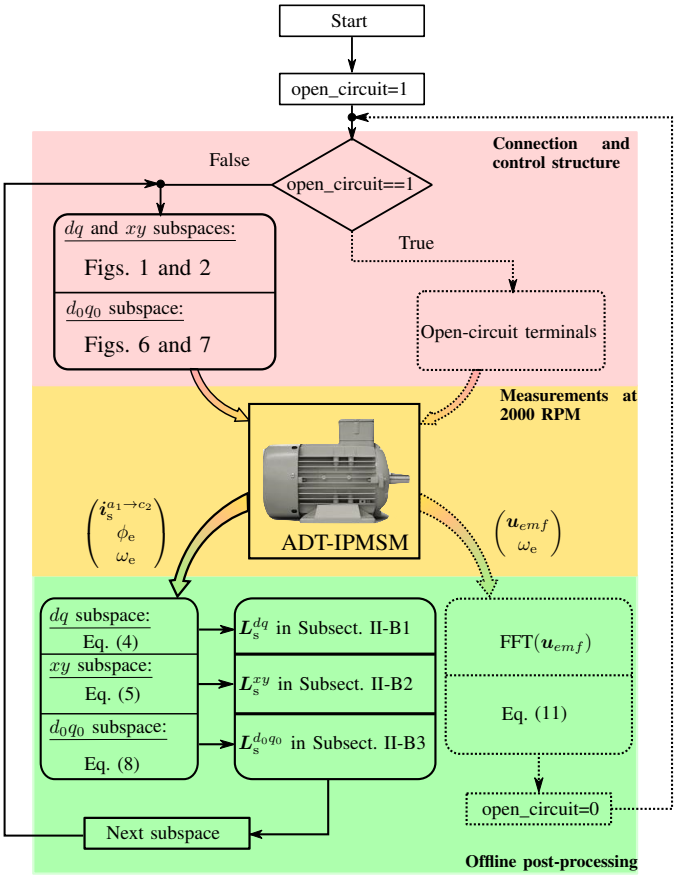

Fig. 10. Flowchart summarizing the sequence to obtain the full parameters of the different subspaces of an ADT-IPMSM in Sect. II-B.

were set to 9 msec, while the proportional part was set to 3 (Ω). As for the *zero* subspace in Fig. 1, the PR controller gains are set similarly to the other two subspaces and are activated only for the 1N connection. Future work will consider model-based parameterization of the PR controller gains using the proposed model.

IV. Evaluation Results

A. Simulation and experimental environments

This section evaluates the outcomes of the proposed model with those implemented on the practical setup shown in Fig. 11. With the aid of Matlab/Simulink, the proposed model in Sect. II has been simulated using the flux linkage maps in Fig. 3 and the corresponding differential inductances in Figs. 4, 5, and 8. The flux linkages where used as the states per each subspace for the carried out simulations, while the corresponding currents where obtained using the inverse interpolation algorithm that extracts the currents $\boldsymbol{i}_{\mathrm{s}}^{dq}$, $\boldsymbol{i}_{\mathrm{s}}^{xy}$ and $\boldsymbol{i}_{\mathrm{s}}^{0}$ from the corresponding flux linkages $\boldsymbol{\psi}_{\mathrm{s}}^{dq}$, $\boldsymbol{\psi}_{\mathrm{s}}^{xy}$, and $\boldsymbol{\psi}_{\mathrm{s}}^{0}$, respectively [16]. Thus, the effect of cross-coupling, saturation, and different machine non-linearities can be included to a high extent. Sampling and switching frequencies are set equal as seen in Table I, where sampling instants are triggered in the middle of the switching period. The control structure was carried out as shown in Fig. 1 and the tuning of the PI controllers were set as in Sec. III. Due to the discrete-time delay, the provided voltage references to the VSIs consider the position error when applying the Park transformation (i.e. $\boldsymbol{T}_p'(\phi_{\mathrm{e}} + \omega_{\mathrm{e}} t_{\mathrm{sw}})$).

The test bench in Fig. 11 consists of an ADT-IPMSM tied to an induction machine acting as the prime mover. The control algorithm is implemented on dSPACE DS1007 by means of Matlab/Simulink interface. The VSIs switching is done via carrier-based pulse-width-modulation (PWM), where the PWM signals are sent to the VSIs via the DS5101 PWM card, which is manually flashed and programmed to ensure precise timings and sampling instants. The A/D DS2004 board is triggered by the DS5101 board to carry-out the measurements in the middle of the switching period, where ϕ_{e}, ω_{e} and $\boldsymbol{i}_{\mathrm{s}}^{a_1 \to c_2}$ are the measured quantities.

B. Steady-state evaluation

This subsection validates the proposed fundamental and harmonic models for 1N and 2N configurations in terms of $\boldsymbol{i}_{\mathrm{s}}^{dq}$ and $\boldsymbol{i}_{\mathrm{s}}^{xy}$, $\boldsymbol{i}_{\mathrm{s}}^{0}$, and $(i_{\mathrm{s}}^{\mathrm{a}_1}, i_{\mathrm{s}}^{\mathrm{a}_2})$ at steady-state at a reference speed of 120 rad/s and $(i_{\mathrm{s,ref}}^{d}, i_{\mathrm{s,ref}}^{q}) = (0, 3)$ A. For the 2N case (i.e. $\boldsymbol{i}_{\mathrm{s}}^{0}$ is discarded), Figs. 12(a)-(b) and 13(a)-(b) represent the outcomes without and with harmonic compensation (HC),

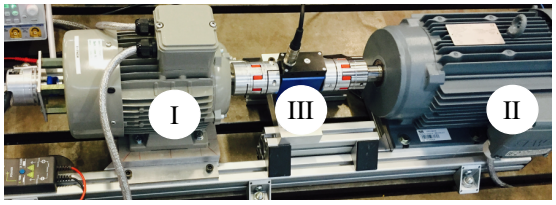

Fig. 11. Test bench: (I) ADT-IPMSM, (II) induction machine (i.e. prime mover) and (III) torque sensor.

TABLE IV. THD and harmonic content of $i_{\mathrm{s}}^{\mathrm{a}_1}$ compared to the fundamental component.

	Order	Simulation		Experimental	
		without HC	HC	without HC	HC
2N	5	20.88%	0.79%	28.91%	0.77%
	7	19.56%	0.28%	28.97%	0.32%
	THD	30.17%	3.06%	41.37%	3.82%
1N	3	17.77%	1.56%	18.1%	0.94%
	5	-	0.77%	-	0.44%
	7	-	0.3%	-	0.58%
	9	6.39%	1.53%	7.12%	0.39%
	THD	19.17%	3.29%	20.1%	4.9%

respectively. If the xy harmonic model presented in Subsect. II-B2 is neglected or unclearly defined [8], [10], the simulations are incapable of generating results similar to those in Fig. 12(a). In terms of total harmonic distortion (THD), simulations indicate that the uncompensated stator currents impose a THD=30.17% compared to the 41.37% obtained by experimental measurements. This anomalous experimental THD is due to the unmodeled non-linearities such as the generated 5^{th} and 7^{th} harmonics by the VSIs; owing to the unmodeled 2μsec fixed dead-time, generated by the gate drivers of the VSIs. Other possible sources of non-linearities are mentioned in [18], [19] such as stator slots mutual coupling, core-losses, and end-turns effects. On the other hand, it is worth to mention that by including the dead-time effect in the simulations, the 5^{th} and 7^{th} harmonics increased, and accordingly, the THD$=$ 35.8%. As for the compensated case, simulations lead to a THD$=$ 3.06% compared to the experimental case THD$=$ 3.82% indicated in Fig. 13. Accordingly, to compare the simulations and experimental measurements for the 1N case, the $\boldsymbol{i}_{\mathrm{s}}^{xy}$ currents were compensated; to overcome the discrepancy between the simulated and experimental harmonic models in the xy plane and its influence on $i_{\mathrm{s}}^{\mathrm{a}_1}$ and $i_{\mathrm{s}}^{\mathrm{a}_2}$. Figs. 14 and 15 illustrate the results without and with HC, respectively, where the simulations were able to adhere to a high extent to the experimental results. The detailed harmonic content and THD for both 1N and 2N cases are shown in Table IV. It is concluded that the proposed simulated harmonic models of the xy and *zero* subspaces coincide with acceptable degree to the experimental waveforms obtained, as illustrated in $\boldsymbol{i}_{\mathrm{s}}^{xy}$ and $\boldsymbol{i}_{\mathrm{s}}^{0}$ in Figs. 12-15.

C. Dynamic evaluation

Since the transient behaviour of ADT-IPMSM is governed by $\boldsymbol{i}_{\mathrm{s}}^{dq}$, the dynamic performance is evaluated through step changes in $\boldsymbol{i}_{\mathrm{s,ref}}^{dq}$ for the 1N case with HC. Figs. 16(a)-(b) plot the simulation and experimental results, respectively, which show the current dynamics and the tracking ability of the imposed $\boldsymbol{i}_{\mathrm{s,ref}}^{dq}$, while illustrating minimum interaction between the i_{s}^{d} and i_{s}^{q}, exhibiting the expected $dq-$decoupling as well as fast transient response [16]. It is worth to mention that the experimental results show slightly higher current ripples, owing to the 11^{th} and 13^{th} harmonics which were not considered in this paper. If desired, one is capable of including such harmonics in the dq frame, where both harmonics are mapped to the 12^{th} harmonic, after applying (2), and expanding the flux linkage equation in Subsect. II-B1; to accommodate the 12^{th} harmonic similar to the method utilized to model the 6^{th} harmonic in the xy subspace in Subsect. II-B2.

V. Conclusion

In this paper an enhanced modelling method has been laid out for ADT-IPMSMs. The proposed modelling of ADT-IPMSM estimates the flux linkages per subspace, from which the differential inductances were identified, taking into account the cross-coupling between the coordinates of the different subspaces as well as saturation. The mapping of the different and significant rotor harmonics in the distinct subspaces has been illustrated, which demonstrated mathematically that harmonic currents are function of the rotary speed. Moreover, a novel connection for estimating the zero sequence flux linkages as well as their differential inductances was presented, capable of exciting only the zero sequence components, while nullifying the currents in the other subspaces. Accordingly, the machine model was identified without prior knowledge of the geometric or design data, relying only on current and speed measurements. The experimentally identified flux linkage maps were also employed in the tuning of the PI current controllers. The proposed model was simulated and assessed against the experimental counterpart on a 2.5 kW ADT-IPMSM, indicating the effectiveness of the proposed method.

Acknowledgment

This work is supported by the project AWESCO (H2020-ITN-642682) funded by the European Union's Horizon 2020 research and innovation program under the Marie Sklodowska-Curie grant agreement No. 642682.

References

[1] I. Gonzalez-Prieto, M. J. Duran, H. S. Che, E. Levi, M. Bermúdez, and F. Barrero, "Fault-tolerant operation of six-phase energy conversion systems with parallel machine-side converters," *IEEE Trans. on Power Electron.*, vol. 31, pp. 3068–3079, April 2016.

[2] Y. Hu, Z. Q. Zhu, and M. Odavic, "Comparison of two-individual current control and vector space decomposition control for dual three-phase pmsm," *IEEE Trans. on Ind. Appl.*, vol. 53, pp. 4483–4492, Sept 2017.

[3] D. Hadiouche, H. Razik, and A. Rezzoug, "On the modeling and design of dual-stator windings to minimize circulating harmonic currents for vsi fed ac machines," *IEEE Trans. on Ind. Appl.*, vol. 40, pp. 506–515, March 2004.

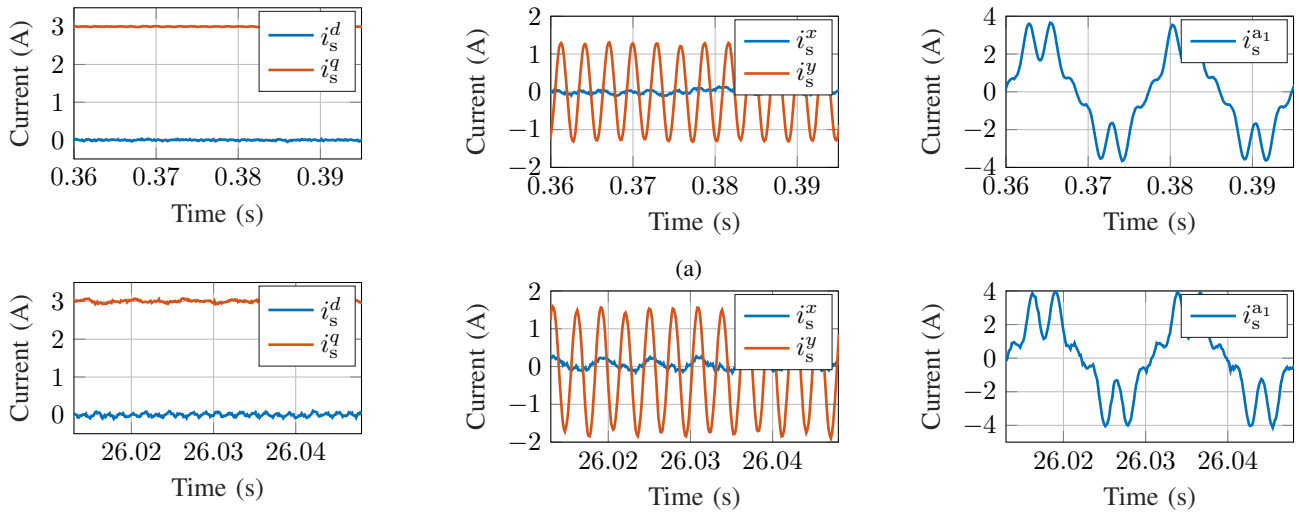

Fig. 12. (a) Simulation and (b) experimental results comparison for the 2N case without $\boldsymbol{i}_s^{xy}$ compensation at steady state for $\boldsymbol{i}_{s,ref}^{dq} = (0,\ 3)^\top$ (A) (left to right): $\boldsymbol{i}_s^{dq}$, $\boldsymbol{i}_s^{xy}$ and $i_s^{a_1}$.

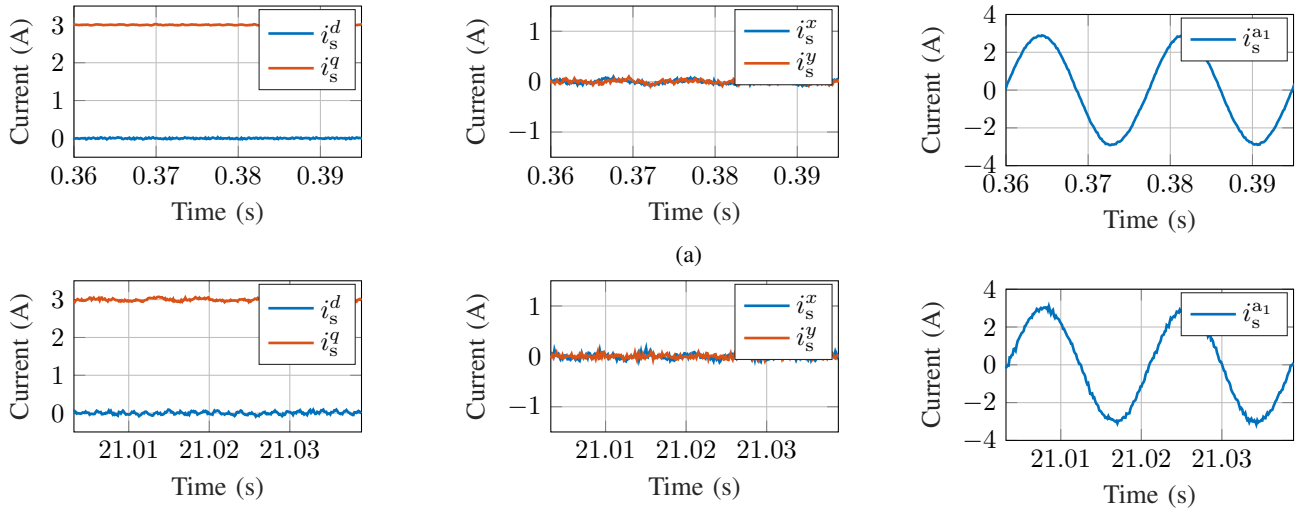

Fig. 13. (a) Simulation and (b) experimental results comparison for the 2N case with $\boldsymbol{i}_s^{xy}$ compensation at steady state for $\boldsymbol{i}_{s,ref}^{dq} = (0,\ 3)^\top$ (A) (left to right): $\boldsymbol{i}_s^{dq}$, $\boldsymbol{i}_s^{xy}$ and $i_s^{a_1}$.

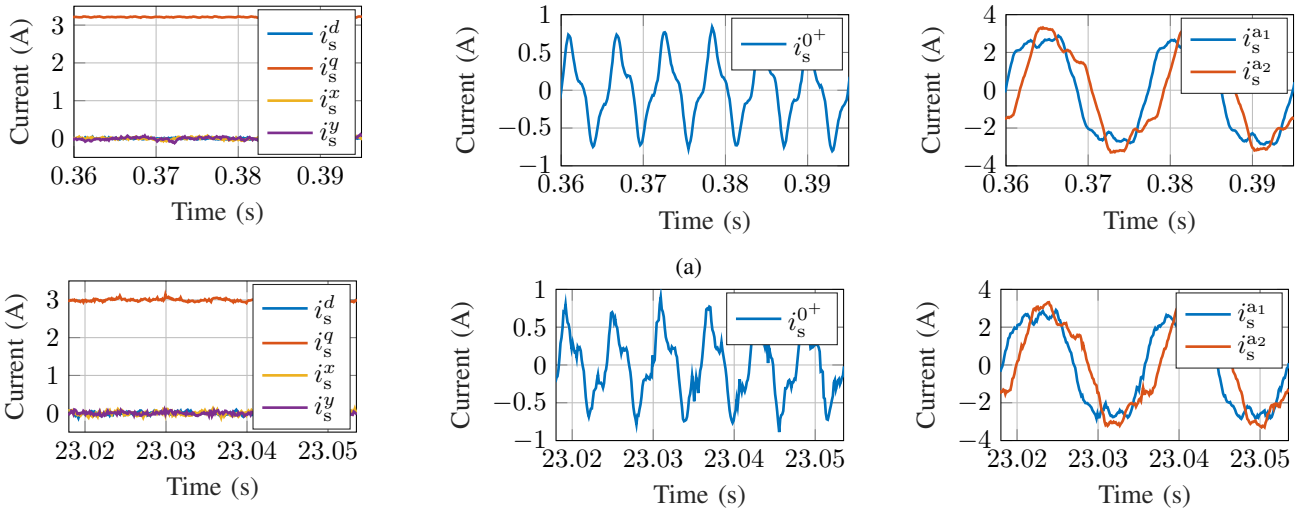

Fig. 14. (a) Simulation and (b) experimental results comparison for the 1N case without $\boldsymbol{i}_s^0$ compensation at steady state for $\boldsymbol{i}_{s,ref}^{dq} = (0,\ 3)^\top$ (A) and $\boldsymbol{i}_{s,ref}^{xy} = (0,\ 0)^\top$ (A) (left to right): $(\boldsymbol{i}_s^{dq},\ \boldsymbol{i}_s^{xy})$, $\boldsymbol{i}_s^0$ and $(i_s^{a_1},\ i_s^{a_2})$.

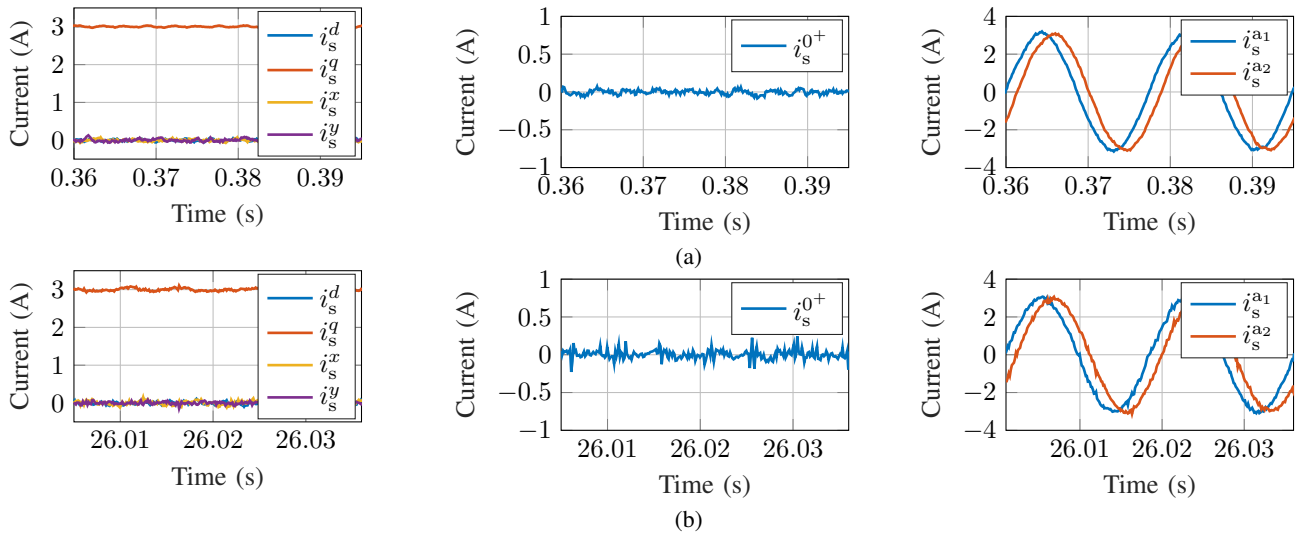

Fig. 15. (a) Simulation and (b) experimental results comparison for the 1N case with $\boldsymbol{i}_s^0$ compensation at steady state for $\boldsymbol{i}_{s,ref}^{dq} = (0, 3)^\top$ (A) and $\boldsymbol{i}_{s,ref}^{xy} = (0, 0)^\top$ (A) (left to right): $(\boldsymbol{i}_s^{dq}, \boldsymbol{i}_s^{xy})$, $\boldsymbol{i}_s^0$ and (i_s^{a1}, i_s^{a2}).

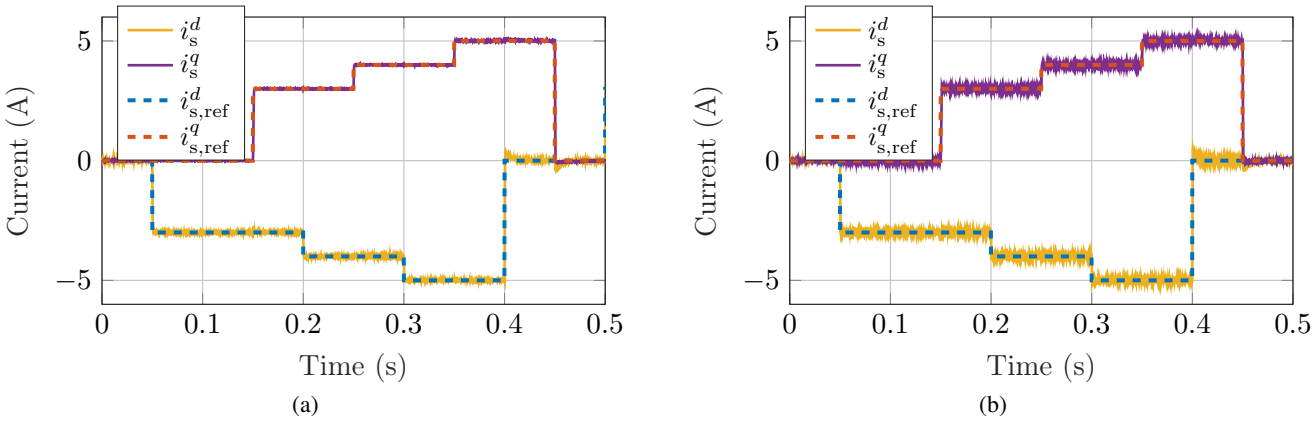

Fig. 16. (a) Simulation and (b) experimental transient response comparison for the 1N case w.r.t. $\boldsymbol{i}_s^{dq}$ with HC at 1200 RPM.

[4] H. S. Che, E. Levi, M. Jones, W. P. Hew, and N. A. Rahim, "Current control methods for an asymmetrical six-phase induction motor drive," *IEEE Trans. on Power Electron.*, vol. 29, pp. 407–417, Jan 2014.

[5] W. N. W. A. Munim, M. Duran, H. S. Che, M. Bermudez, I. Gonzalez-Prieto, and N. A. Rahim, "A unified analysis of the fault tolerance capability in six-phase induction motor drive," *IEEE Trans. on Power Electron.*, vol. 32, no. 10, pp. 7824–7836, 2016.

[6] S. Hu, Z. Liang, W. Zhang, and X. He, "Research on the integration of hybrid energy storage system and dual three-phase pmsm drive in ev," *IEEE Trans. on Ind. Electron.*, 2017 (early-access).

[7] H. S. Che, A. S. Abdel-Khalik, O. Dordevic, and E. Levi, "Parameter estimation of asymmetrical six-phase induction machines using modified standard tests," *IEEE Trans. on Ind. Electron.*, vol. 64, no. 8, pp. 6075–6085, 2017.

[8] Y. Hu, Z. Q. Zhu, and K. Liu, "Current control for dual three-phase permanent magnet synchronous motors accounting for current unbalance and harmonics," *IEEE Journal of Emerging and Selected Topics in Power Electron.*, vol. 2, pp. 272–284, June 2014.

[9] A. G. Yepes, J. Doval-Gandoy, F. Baneira, D. Perez-Estevez, and O. Lopez, "Current harmonic compensation for n-phase machines with asymmetrical winding arrangement and different neutral configurations," *IEEE Trans. on Ind. Appl.*, vol. PP, no. 99, pp. 1–1, 2017.

[10] S. Kallio, M. Andriollo, A. Tortella, and J. Karttunen, "Decoupled d-q model of double-star interior-permanent-magnet synchronous machines," *IEEE Trans. on Ind. Electron.*, vol. 60, pp. 2486–2494, June 2013.

[11] M. H. Vafaie, B. M. Dehkordi, P. Moallem, and A. Kiyoumarsi, "Minimizing torque and flux ripples and improving dynamic response of pmsm using a voltage vector with optimal parameters," *IEEE Trans. on Ind. Electron.*, vol. 63, pp. 3876–3888, June 2016.

[12] R. Cai, R. Zheng, M. Liu, and M. Li, "Robust control of pmsm using geometric model reduction and μ-synthesis," *IEEE Trans. on Ind. Electron.*, vol. 65, pp. 498–509, Jan 2018.

[13] W. Wang, J. Zhang, M. Cheng, and S. Li, "Fault-tolerant control of dual three-phase permanent-magnet synchronous machine drives under open-phase faults," *IEEE Trans. on Power Electron.*, vol. 32, pp. 2052–2063, March 2017.

[14] S. Kallio, J. Karttunen, P. Peltoniemi, P. Silventoinen, and O. Pyrhonen, "Determination of the inductance parameters for the decoupled d-q model of double-star permanent magnet synchronous machines," *IET Electric Power Appl.*, vol. 8, pp. 39–49, Feb. 2014.

[15] C. M. Hackl, *Non-identifier based adaptive control in mechatronics: Theory and Application*. No. 466 in Lecture Notes in Control and Information Sciences, Berlin: Springer International Publishing, 2017.

[16] C. M. Hackl, M. J. Kamper, J. Kullick, and J. Mitchell, "Current control of reluctance synchronous machines with online adjustment of the controller parameters," in *in Proceedings of the 2016 IEEE International Symposium on Ind. Electron. (ISIE 2016)*, (Santa Clara, CA, USA), pp. 156–160, 2016.

[17] K. Marouani, L. Baghli, D. Hadiouche, A. Kheloui, and A. Rezzoug, "A new pwm strategy based on a 24-sector vector space decomposition for a six-phase vsi-fed dual stator induction motor," *IEEE Trans. on Ind. Electron.*, vol. 55, pp. 1910–1920, May 2008.

[18] Y. Zhao and T. A. Lipo, "Space vector pwm control of dual three-phase induction machine using vector space decomposition," *IEEE Trans. on Ind. Appl.*, vol. 31, pp. 1100–1109, Sep 1995.

[19] T. Lipo, "A d-q model for six phase induction machines," in *Proceedings of the Int. Conf. Electric Machines*, pp. 860–867, 1980.

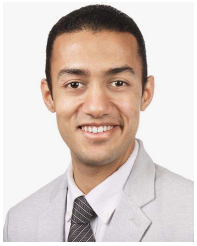

Hisham M. Eldeeb received his B.Sc. (honors) and M.Sc. in electrical engineering in 2011, 2014, respectively, from the Faculty of Engineering, Alexandria University, Egypt. From 2012 to 2015, he worked as a research associate at the College of Engineering, Qatar University in Qatar, where he was hired on 1.4M$ project; aiming at extending the amount of penetration of inverter-based distributed-generation plants within the Qatari-Network. From September 2015, he was selected as one of the 14 Marie-Curie Ph.D. candidates hired on the 3M€ EU Horizon H2020 project "Airborne wind energy system control and optimization" (AWESCO). He is currently working towards his Ph.D. degree at the Technical University of Munich, Germany. His research interests are grid-connected converters, power quality issues, power electronics, electrical drives, and optimal control.

Ayman S. Abdel-Khalik (SM'12) received the B.Sc. and M.Sc. degrees in electrical engineering from Alexandria University, Alexandria, Egypt, in 2001 and 2004, respectively, and the Ph.D. degree in electrical engineering from Alexandria University, and Strathclyde University, Glasgow, U.K., in 2009, under a dual channel program. He was with Spiretronic LLC, Houston, TX, USA, as a Senior Research Scientist from 2009 to 2014. From 2015 to 2017, he was an Associate Research Scientist with Texas A&M University at Qatar, Doha, Qatar. He is currently an Associate Professor with the Electrical Engineering Department, Faculty of Engineering, Alexandria University, Alexandria, Egypt. His current research interests include electrical machine design, electric machine simulation, electric drives, energy conversion, and renewable energy.

Christoph M. Hackl (M'12 - SM'16) was born in 1977 in Mannheim, Germany. After studying electrical engineering (controls and mechatronics) at Technical University of Munich (TUM, Germany) and University of Wisconsin-Madison (USA), he received the B.Sc., Dipl.-Ing., and Dr.-Ing. (Ph.D.) degree in 2003, 2004 and 2012 from TUM, respectively. Since 2004, he is teaching electrical drives, power electronics, and mechatronic & renewable energy systems. Since 2014, he is heading the research group "Control of Renewable Energy Systems (CRES)" at TUM. In February 2018, he has been appointed Professor for Electrical Machines and Drives at the Munich University of Applied Sciences (MUAS), Germany. His main research interests are nonlinear, adaptive and optimal control of electric, mechatronic and renewable energy systems.